ACS OMEGA

Open Access

http://pubs.acs.org/journal/acsodf

Article

Repurposing Oseltamivir Against CAG Repeat Mediated Toxicity in Huntington's Disease and Spinocerebellar Ataxia Using Cellular and *Drosophila* Model

Krishna Singh,[†] Kanav Gupta,[†] Sakshi Shukla,[†] Aditi Pramod Kumari, and Amit Kumar*

Cite This: *ACS Omega* 2025, 10, 14980−14993

Read Online

ACCESS | Metrics & More | Article Recommendations | Supporting Information

ABSTRACT: Huntington's disease (HD) and Spinocerebellar Ataxia (SCA) are debilitating neurological disorders triggered by the expansion of CAG sequences within the specific genes (HTT and ATXN, respectively). These are characterized as poly glutamine (polyQ) disorders, which are marked by widespread neurodegeneration and metabolic irregularities across systemic, cellular, and intracellular levels. This study aimed to identify small molecules that specifically interact with and target the toxic CAG repeat RNA. Here, we investigated the neuroprotective effects of Oseltamivir, an antiviral drug, against the HD and SCA-causing CAG repeats, through biophysical, cellular, and *Drosophila* model-based studies. Using a multidimensional approach encompassing biophysical techniques, cellular assays, and a *Drosophila* model, we explored Oseltamivir's interaction with toxic CAG repeat RNA. Our comprehensive analyses, including circular dichroism (CD), isothermal titration calorimetry (ITC), electrophoretic mobility shift assay (EMSA), and nuclear magnetic resonance (NMR) spectroscopy, demonstrated Oseltamivir's specific binding affinity for AA mismatches and its potential to mitigate the toxicity associated with polyQ aggregation. Moreover, the identified U.S. FDA-approved drug effectively mitigated polyQ-induced toxicity in both HD cells and the *Drosophila* model of the disease. The results obtained from this drug repurposing approach are indicative of the neuro-shielding role of Oseltamivir in HD and several SCAs, paving the way for its translation into clinical practice to benefit patients afflicted with these devastating diseases.

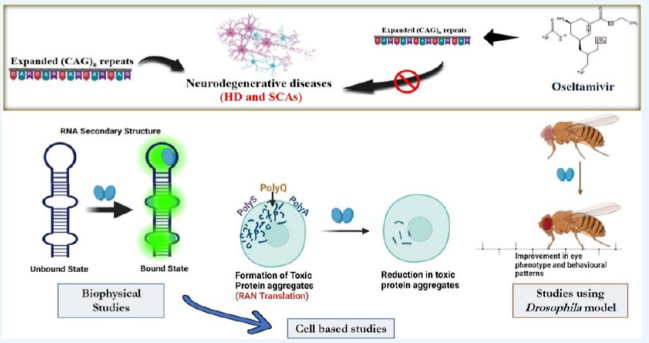

INTRODUCTION

RNA's potential as a therapeutic intervention target has recently highlighted its significance in neuropharmacology, particularly regarding trinucleotide repeat expansion disorders (TREDs) and their role in causing numerous neurodegenerative and neuromuscular disorders.[1] More than 50 disorders stem from aberrant nucleotide sequence amplification within genes, with over 20 attributed exclusively to trinucleotide repeat expansions,[2] such as Huntington's Disease (HD), Fragile X Syndrome (FXS), and various Spinocerebellar Ataxias (SCAs).[3−7] These expansions can occur in 5′ UTR, exons, introns, and 3′ UTR regions of the genes. TREDs result from triplet repeat expansions surpassing a threshold. For instance, when the CAG motif expands beyond 37 repeats, it results in the onset of HD, a perilous condition with a rapidly evolving landscape, posing a significant and concerning challenge.[8] Consequently, neurons become impaired and ultimately undergo cell death, resulting in choreiform movements, cognitive deterioration, and psychiatric disorders.[9] Disease severity correlates positively with repeat number, resulting in complete penetrance.[10] The associated symptoms range from involuntary movements to motor abnormalities and hyperkinetic movements.[11,12]

TREDs primarily disrupt cellular functions through four pathogenic pathways: sequestration of essential proteins (e.g., MBNL1, DICER), transcriptional silencing (e.g., FXS), toxic protein aggregation (e.g., HD), and repeat-associated non-ATG (RAN) translation.[13] HD pathology involves several critical aspects: abnormal protein aggregation, proteolytic cleavage, neuronal damage, disrupted transcription, compromised autophagy, and mitochondrial abnormalities.[14] The mutant huntingtin protein (mHTT) in HD forms aggregates due to an extended poly glutamine tract (polyQ), causing cellular toxicity. Additionally, expanded CAG repeats initiate a pathogenic cascade via RAN translation, producing various homopolymeric proteins such as poly-Ala, poly-Cys, poly-Ser, and poly-Leu.[15,16] Current treatments for HD are limited to alleviating its symptomatic effects, with no therapies available as of now to

Received: November 14, 2024
Revised: February 12, 2025
Accepted: February 18, 2025
Published: February 22, 2025

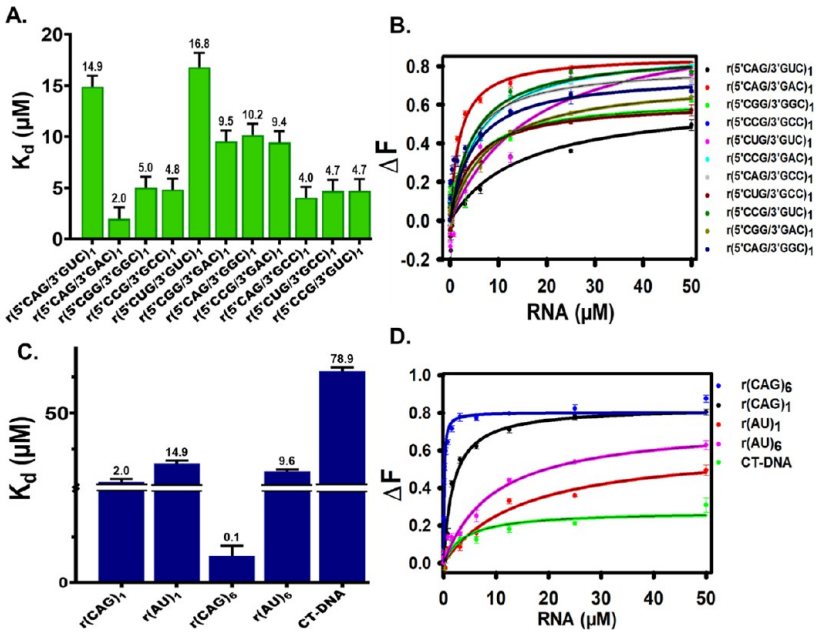

Figure 1. Evaluation of the binding affinity of Oseltamivir drug with nucleic acids. (A) Bar graph denoting K_d values of (5′C**N**G/3′G**N**C) RNA motifs with Oseltamivir. (B) The plot represents fluorescence titration assay one-mode curve fitting of (5′C**N**G/3′G**N**C) RNA motifs with Oseltamivir. (C) The bar graph represents the K_d value analysis of different RNA and DNA controls with the Oseltamivir. (D) The plot depicts fluorescence titration assay one-mode curve fitting of r(C**A**G)$_{exp}$ RNAs and different RNA and DNA controls with Oseltamivir. Error bars represent the standard deviation (n = 3).

counteract its onset or effectively slow the disease progression.[17] Conventional treatments aim to mitigate mutant protein aggregation using methods like antisense oligonucleotides (ASO), caspase 6 inhibitors, RNAi, zinc finger motif proteins, CRISPR-Cas9, etc.[18,19] However, these strategies face challenges such as immune reactions, inadequate medication administration, and the blood−brain barrier, limiting clinical success.[20]

To surmount these challenges, researchers are currently investigating small molecule-based treatments as a strategy, which offer benefits like better brain penetration, lower immunogenicity, and potential oral administration. These small molecules target repetitive RNAs and microRNAs, modifying their activities and addressing the underlying molecular abnormalities.[21−23] Targeting r(C**A**G)$_{exp}$ RNA could be more effective than focusing on mutant proteins, providing a direct way to intervene in the disease pathogenesis and enabling personalized medicine. Ongoing research aims to refine these treatments through structural biology and in vivo studies.

This study utilized a drug repurposing approach to identify U.S. FDA-approved small molecules with lower cytotoxicity, higher binding affinity and selectivity toward C**A**G repeat RNA. Oseltamivir, effective in preventing influenza complications and potentially useful for liver cancer treatment, was explored for its therapeutic effects against HD.[24,25] We investigated its ability to influence r(C**A**G)$_{exp}$ RNA structure and function using fluorescence-based methods and various biophysical techniques like isothermal calorimetry titration (ITC), circular dichroism (CD) spectroscopy, electrophoretic mobility gel shift assay (EMSA), and polymerase chain reaction stop assays. Our results confirmed Oseltamivir's binding potential and selectivity to multiple C**A**G repeat RNAs, followed by similar significant outcomes from the cell-based approaches. Further, this study majorly utilized a *Drosophila* model of polyQ diseases to evaluate the effectiveness of Oseltamivir in mitigating the disease symptoms. Transgenic *Drosophila* models have proven highly effective in neurodegenerative disease research, faithfully reproducing key aspects such as late-onset symptoms, shortened lifespan, neurodegeneration, motor dysfunction, and the gradual buildup of aggregates in the cytoplasm and neurites.[26]

This study reveals that Oseltamivir reduced polyQ protein aggregates and improved cell viability in both the HD cellular and *Drosophila* models, indicating its potential as a therapeutic agent for HD and several SCAs. It has been found to preserve the standard internal eye architecture in the transgenic *Drosophila* expressing Httex1pQ93. Additionally, the drug molecules improved the extensive dysmorphology and degeneration of the diseased fly's eye, motor functions, and the prevalence of apoptotic cell death. The administration of Oseltamivir to the HD *Drosophila* model thus significantly mitigates the pathological phenotype induced by the toxic C**A**G repeats. These findings thus highlight its potential as a neuroprotective agent in HD and SCA, offering hope for its use in slowing down their progression.

RESULTS AND DISCUSSION

The drug development landscape has been transformed in recent decades with the discovery and design of RNA-based therapeutics. The effectiveness of this approach has been most clearly demonstrated by antibiotic medications that interact with bacterial rRNA. This observation has sparked interest in targeting atypical cellular RNAs linked to pathological states. Expanded repeat RNAs have emerged as promising targets for treating various neurological and neuromuscular disorders, such as FXTAS, HD, and several SCAs. This study investigated Oseltamivir, an FDA-approved small molecule, as a potent compound selectively targeting the r(C**A**G)$_{exp}$ RNA.

Investigating the Binding of Oseltamivir to 1 × 1 RNA Motifs and r(CA**G)$_{exp}$ RNAs.** Given the potential of r(C**A**G)$_{exp}$

https://doi.org/10.1021/acsomega.4c10338
ACS Omega 2025, 10, 14980−14993

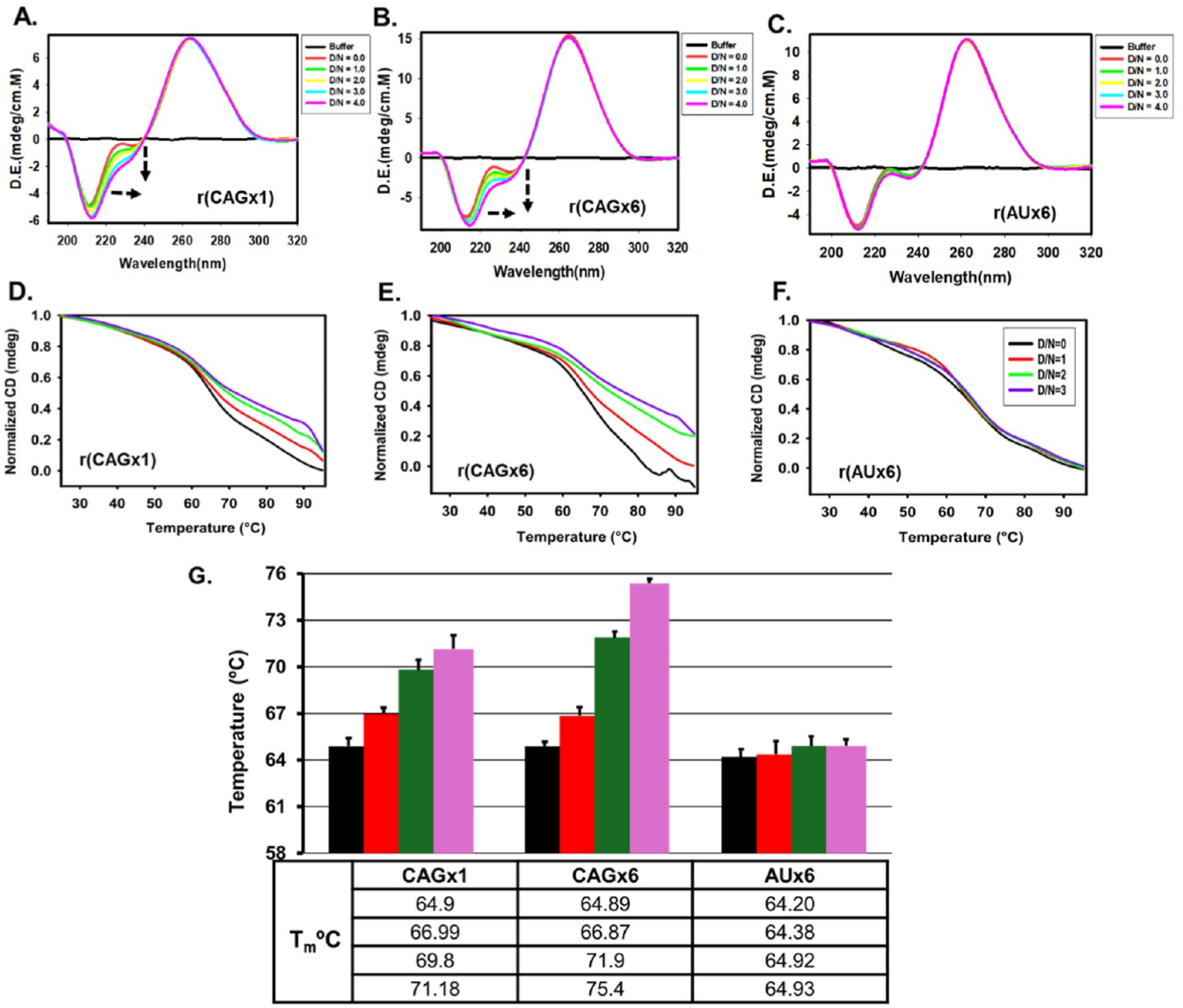

	CAGx1	CAGx6	AUx6
T_m°C	64.9	64.89	64.20
	66.99	66.87	64.38
	69.8	71.9	64.92
	71.18	75.4	64.93

Figure 2. Circular dichroism spectroscopy titration of r(C**A**G)$_{exp}$ and r(AU)$_{exp}$ duplex RNAs in the presence of Oseltamivir. (A) r(C**A**Gx1), (B) r(C**A**Gx6), (C) r(AUx6) RNA. CD thermal profile of (D) r(C**A**Gx1), (E) r(C**A**Gx6), (F) r(AUx6) RNA with Oseltamivir. (G) The bar graph represents the changes in melting temperature of the r(C**A**Gx1), r(C**A**Gx6), and r(AUx6) RNA motifs with varying drug concentrations. D/N denotes the drug-to-nucleotide ratio. Error bar indicates standard deviation. Data were obtained from 3 independent samples (n = 3).

RNA as a therapeutic target, we initially assessed Oseltamivir's binding affinity to different r(C**N**G)$_{exp}$ RNA motifs. Through fluorescence titration assays, we examined the interaction of Oseltamivir with all the possible combinations of 5′C**N**G/3′G**N**C RNA motifs, where N represents A, U, C, and G bases. These trinucleotides repeat RNA motifs are flanked by GC bases, facilitating proper RNA hairpin folding. The gradual addition of RNA to the Oseltamivir solution resulted in a gradual increase in fluorescence intensity at the emission maxima of Oseltamivir, indicating the formation of an RNA-Oseltamivir complex. Plotting the change in fluorescence intensity against RNA concentration provided the binding constant values, revealing the binding affinity of Oseltamivir for each RNA (Figure 1A−D).

Notably, Oseltamivir exhibited higher binding affinity and selectivity for AA-rich (5′C**A**G/3′G**A**C) RNA motifs compared to other mismatched RNA motifs and the 5′C**A**G/3′G**U**C (AU paired) RNA, which served as a control (Figures 1B, S1, S2 and Table S1). The varying binding behavior of Oseltamivir with different RNA motifs may arise from differences in binding affinity among the various repeat sequences and the topological disparities between these RNAs. However, the strong affinity and selectivity of Oseltamivir for (5′C**A**G/3′G**A**C) RNA motifs over other RNAs prompted further investigation of its binding behavior with (5′C**A**G/3′G**A**C) RNA containing a high number of C**A**G repeats, i.e., C**A**Gx6 RNA.

As expected, stronger affinity was observed for these large repeat AA-rich motif RNAs. Additionally, the drug molecule displayed selectivity for C**A**G RNA over other fully base-paired AU × 6 RNA, exhibiting approximately 86-fold higher affinity for the r(C**A**G)$_6$ repeat RNA (Figures 1D, S3 and Table S1). r(CGG)$_{exp}$, r(CCG)$_{exp}$, and r(CUG)$_{exp}$ also form GG, CC, and UU 1 × 1 internal hairpin structures, respectively. Binding studies demonstrate that Oseltamivir binds more specifically with CAG repeat RNA than with other mismatched RNA motifs (Figures 1B, S1 and Table S1). Furthermore, to assess the

https://doi.org/10.1021/acsomega.4c10338
ACS Omega 2025, 10, 14980−14993

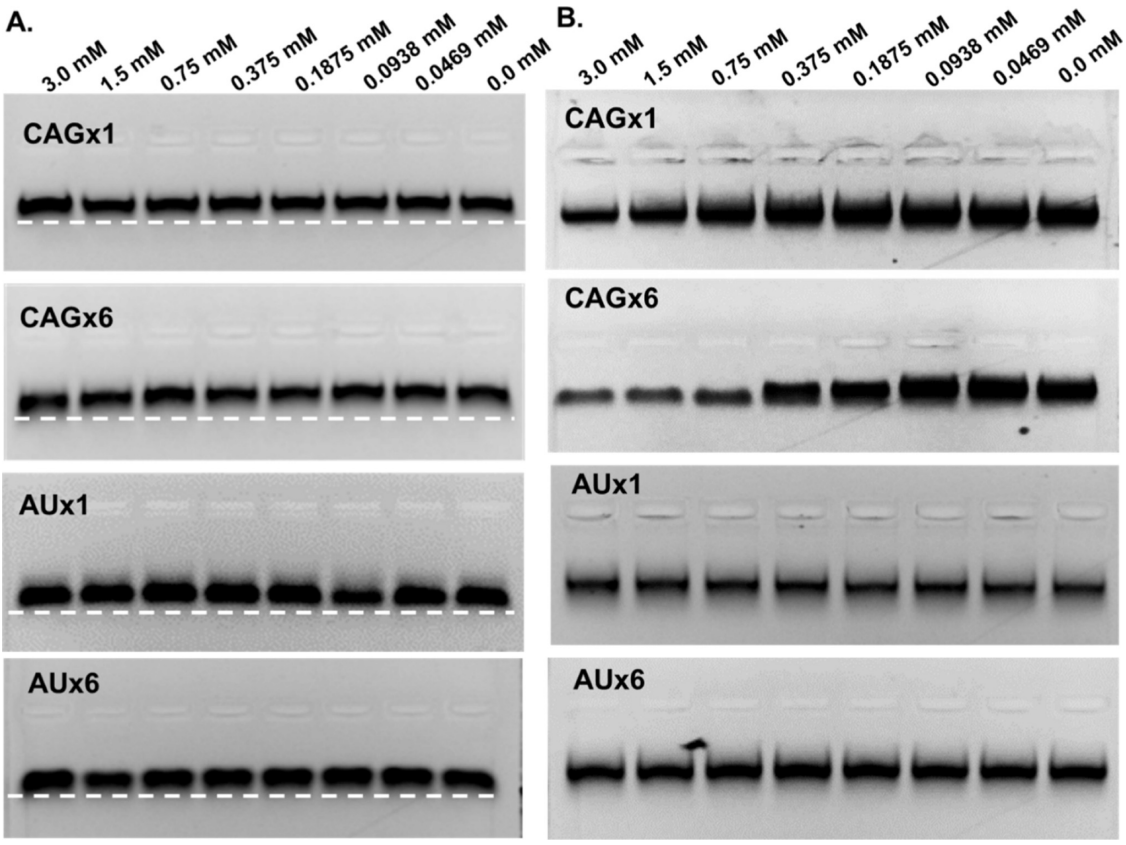

Figure 3. Gel retardation assay and PCR stop assay. (A) Gel retardation images show that with an increasing concentration of Oseltamivir, the mobility of C**A**G repeat RNAs significantly increases over AU duplex RNA. (B) Gel images show the decreased intensity of the PCR product with increasing concentration of Oseltamivir compared with the AU-paired template.

potential applicability of Oseltamivir-based therapeutics, the binding affinity of Oseltamivir was also evaluated against duplex calf thymus (CT) DNA present in cells (Figures 1C,D and S3C). While it interacted with the CT-DNA sequence, its affinity was approximately 700-fold lower than the binding affinity of r(C**A**Gx6) RNA (Table S1).

We further conducted ITC experiments to validate the binding affinity of Oseltamivir with r(C**A**Gx6) and r(AUx6) RNA motifs. The data were analyzed using a two-site binding model for both RNAs. The observed exothermic peaks are attributed to the increased interaction between Oseltamivir and r(C**A**Gx6) RNA. The dissociation constants obtained for the AA and AU pairs were 707 nM and 0.180 mM, respectively (Figure S4 and Table S2). This indicates a stronger affinity and specificity of Oseltamivir for the AA motif-containing RNA compared to the control, AU-paired duplex RNA. These results confirm robust and high binding, supporting the nanomolar range of binding observed in the fluorescence binding assay with the r(C**A**Gx6) motif-RNA.

Circular Dichroism Spectroscopy Evaluates the Topological Effects of Binding of the Lead Molecule to RNA. To investigate how the Oseltamivir drug molecule's binding influences the loop structures in RNA that arise from mismatched bases, we employed CD spectroscopy. This study particularly examined RNA sequences with AA mismatches. RNA with standard A-U base pairing was also compared to the mismatched pairs to evaluate the drug molecule's selectivity and specificity. CD spectra of RNA containing r(C**A**Gx1) and r(C**A**Gx6) showed a prominent positive peak at around 270 nm and a smaller peak at around 240 nm, which was consistent with double-stranded A-form structures.[27,28] With the addition of Oseltamivir up to a D/N ratio of 4.0, the intensity of the positive peak did not change. However, a hyperchromic shift and red shift in the negative peak were observed, whereas the overall RNA structure was found to remain the same, defining the stabilizing effect of the Oseltamivir molecule on binding with the AA mismatch. This defined a change in the interactions of the motif RNA with the small molecule. The change was more profound in the RNA motif containing six (AA) mismatches, showing more vital molecule interaction with the RNA as the number of repeats increased (Figure 2A−C). Since the negative peak is base-stacking sensitive, an increase in its intensity might be interpreted as a change in base-stacking in RNA, while RNA's overall conformation stayed the same. Furthermore, no modifications were seen for paired AU-RNA; this change exclusively occurs in the AA mismatch containing RNA motifs.

We also conducted CD melting experiments on RNA and its complex with Oseltamivir to study the folding pattern of RNA as a function of temperature. The CD melting curves were recorded at a wavelength of 260 nm for all CAG repeat RNAs up to a ratio of D/N = 3.0. On subjecting Oseltamivir at 3.0 molar ratio, the change in melting temperature (ΔT_m) was observed as 6.28 and 10.51 °C for r(C**A**Gx1) and r(C**A**Gx6) respectively (Figure 2D,E). However, no change in T_m was observed with AU-paired RNA (Figure 2F). Oseltamivir thus enhanced the melting temperature of expanded C**A**G RNAs, whereas no significant change in T_m was observed with other mismatched RNA motifs or AU duplex RNA (Figure 2). Thermal profile data, therefore, implies that Oseltamivir strongly and selectively interacts with C**A**G repeats RNA and

https://doi.org/10.1021/acsomega.4c10338
ACS Omega 2025, 10, 14980−14993

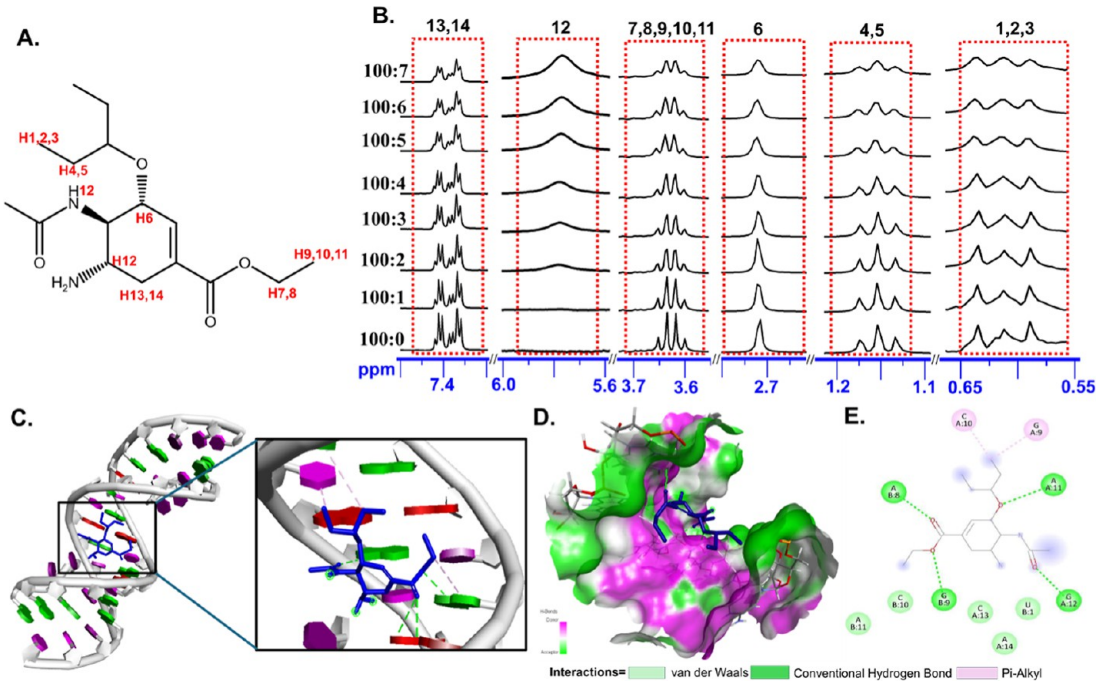

Figure 4. Structural insight into the interaction of 5′r(C**A**Gx6)3′ repeat RNA with Oseltamivir using 1D ^{1}H NMR spectroscopy. One dimensional proton spectra of Oseltamivir as a function of increasing concentration of RNA 5′r(C**A**Gx6)3′. (A) Marked protons of Oseltamivir taking part in interaction with C**A**G repeat RNA motif. (B) Titration of oseltamivir with 5′r(C**A**Gx6)3′ repeat RNA (0.55−7.8 ppm). (C−E) Docking study of Oseltamivir with C**A**G RNA, (C) molecular interaction of Oseltamivir with C**A**G RNA without surfaces, (D) 3D molecular interaction of Oseltamivir with C**A**G RNA, and (E) 2D molecular interaction of Oseltamivir with C**A**G RNA.

forms a stable complex over AUx6 duplex control RNA. These results were in line with the CD spectra results and corroborated the specific binding of Oseltamivir with (5′C**A**G/3′G**A**C) RNAs (Figure 2G).

Electrophoretic Mobility Shift and Polymerase Chain Reaction Inhibition Assay of r(CAG)$_{exp}$ RNAs with Oseltamivir. We further conducted PCR stop and EMSA to validate our above-mentioned findings. EMSA is an essential tool for verifying the specificity and selectivity of the primary molecule with the RNA motif. The obtained results show that all r(C**A**G)$_{exp}$ RNAs had migration acceleration upon interaction with Oseltamivir. The most notable migration acceleration was seen in higher repeat C**A**G RNAs, such as r(C**A**Gx6) (Figure 3A). This acceleration in migration suggests that the drug enhances the RNA motif's stability. This observation aligns with the findings from CD spectroscopy, which indicates that the Oseltamivir molecule stabilizes the loop's double-stranded hairpin structure. The increased stability results in a more compact macromolecule that migrates through the gel more rapidly than the unbound RNA. However, AU paired duplex RNA and higher repeat AU paired duplex RNA containing 6 repeats did not exhibit any migratory retardation or acceleration, confirming Oseltamivir's preferential binding to r(C**A**G)$_{exp}$ RNAs, specifically in terms of correlation between increasing drug concentration and migration (Figure 3A). Additionally, the shift observed in relation to canonical paired RNA is significant, with a p-value of 0.001614, which is less than 0.01. This indicates a 99% confidence level that Oseltamivir interacts with AA mismatched RNA rather than canonical paired RNA. A significant shift was also seen in the case of r(C**A**Gx1), with a p-value of 0.0065 (Figures S6 and S14).

Concurrently, we also investigated the binding of Oseltamivir to C**A**G repeats using PCR stop assays. This aimed to ascertain Oseltamivir's interaction with C**A**G repeats and its potential to inhibit polymerase activity during extension. In accordance with this hypothesis, the PCR product's band intensity diminished with the further addition of Oseltamivir. The binding of the drug molecules with the template-containing loops thus leads to hindrance in the activity of the Taq polymerase, which leads to a reduction in the amplification of the template.

As per the gel images of the PCR stop assay performed for the template r(C**A**Gx1), r(C**A**Gx6), r(AUx1), and r(AUx6), it is clearly evident that with increasing concentration of Oseltamivir, the amplified PCR products as identified by the intensity of bands has decreased significantly, whereas no significant decrease was observed for the canonically paired duplex control amplification, specifying the selectivity of the Oseltamivir molecule to bind with AA mismatch containing nucleic acids (Figure 3B). We also conducted an EMSA and PCR stop assay using r(CAG)$_6$ with pyridostatin (PDS) as a control. PDS is specific to G-quadruplex structures and therefore does not interact with sequences that form hairpin structures. Consequently, no changes in mobility or band intensity were observed with PDS (Figure S14C,D). This affirms the specificity of Oseltamivir for hairpin structures forming CAG repeats. Further analysis was conducted using ImageJ software to ascertain the differences between each set, as shown in the bar graph (Figure S5). After analysis, a significant decrease in the intensity of bands for AA mismatched DNA is observed with a p-value of 0.002879 < 0.1.

Understanding the Binding of Oseltamivir to CA**G × 6 Motif-Containing RNA by NMR Spectroscopy.** A one-dimensional (1D) proton NMR titration was conducted to investigate the interactions between RNA and Oseltamivir at an atomic resolution. This technique enabled the examination of NMR line broadening of drug resonances as RNA was

https://doi.org/10.1021/acsomega.4c10338
ACS Omega 2025, 10, 14980−14993

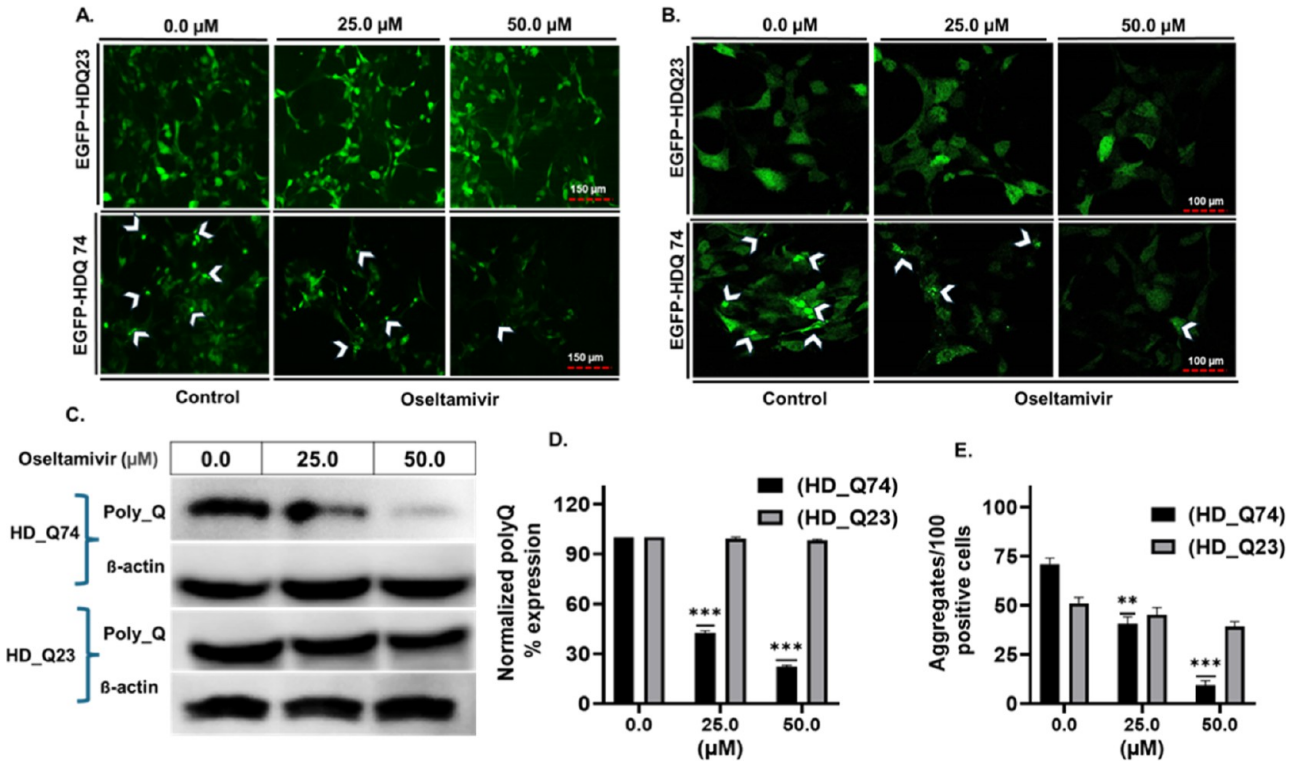

Figure 5. Aggregate formation in cells transfected with normal (EGFP-HDQ23) and expanded polyQ constructs (EGFP-HDQ74) were observed under a fluorescence microscope. (A) Scale bar 150 μM. (B) Scale bar 100 μm. The arrowhead represents the presence of aggregates. Aggregate formation was analyzed on treatment with Oseltamivir for a duration of 24 h. (C) Blot represents a reduction of PolyQ expression following treatment with Oseltamivir. (D,E) Quantitative analysis of the normalized PolyQ protein expression and aggregate formation, respectively. Standard deviation is denoted by error bars. A one-way ANOVA test was used to determine the statistical significance by comparing PolyG aggregate reduction in treated cells to untreated cells ($^*P < 0.05$, $^{**}P < 0.01$, and $^{***}P < 0.001$, $n > 3$).

incrementally added, offering structural insights into how drug molecule's protons behave in their free and bound states. Notably, peaks observed at approximately 1.20 and 0.60 ppm, which correspond to aliphatic protons (H1−H5) of methyl (−CH_3) and methylene (−CH_2−) groups, exhibited noticeable changes. In addition, peaks at 3.60 and 2.70 ppm are associated with protons (H7−H11) that are attached to electronegative atoms such as oxygen or nitrogen (e.g., NH_2, −OCH_3, or C═O). Peaks at 7.35 ppm, attributed to protons (H13, H14), showed progressive attenuation. The disappearance of these proton signals became particularly pronounced at a 100:7 drug-to-RNA molar ratio, indicating specific interactions and structural perturbations in the drug upon binding with RNA (Figure 4B). The analysis of the proton NMR spectra suggests that the drug molecule interacts with the target RNA at multiple binding sites, involving both aliphatic and aromatic regions.

Peaks at 1.20 and 0.60 ppm, corresponding to aliphatic protons, and at 3.60 and 2.70 ppm, associated with protons near electronegative atoms, demonstrate changes indicative of hydrophobic interactions. Additionally, signals at 7.35 and 5.75 ppm attributed to vinylic protons and protons in hydroxyl (−OH) or amide (−NH) environments reveal deshielding effects consistent with interactions between the drug and the target RNA. Notably, the emerging peak at 5.75 ppm suggests the formation of hydrogen bonds facilitated by the drug molecule, further contributing to the binding specificity. These findings highlight the multifaceted nature of the interactions, which include hydrophobic forces, electrostatic interactions, and hydrogen bonding. Understanding these binding mechanisms provides valuable insights for rationalizing RNA-targeted therapeutic strategies.

In Silico Interaction Studies Using Molecular Docking and MD Simulations. To append our findings from the biophysical experiments, docking analysis was performed to generate models of drug-RNA complex in-silico. Our mismatch AA RNA motif was found to interact with the drug molecules. After docking the Oseltamivir molecule with the duplex RNA complex (PDB id: 4J50), the best-predicted pose had a binding affinity of −6.1 kcal/mol. The presence of 3 C**A**G repeats causes the strong interaction between the molecule and duplex, mainly the A8 and A11 in the RNA duplex complex, to form conventional hydrogen bonds with drug molecules, justifying the interaction of the molecules at the AA mismatch loop and preliminary in vitro studies (Figure 4C−E).

Further, a molecular dynamic simulation of a docked model of the Oseltamivir-RNA complex was performed. Following a 100 ns long molecular dynamics simulation, the trajectory was examined to evaluate the stability of the RNA-ligand complex. The root-mean-square deviation (RMSD) shows the structural variations in the dynamic trajectory. The consistent RMSD observed in molecular dynamics (MD) simulation confirmed the stable nature of the RNA-ligand complexes (Figure S7). Further comparisons between the RMSD of RNA and complex show the complex to be more stable than only RNA. This further indicates the stable nature of the interactions between the RNA and the small molecule.

The overall stability of RNA is also increased as compared to RNA alone, as observed through a decrease in periodic fluctuations as well as the intensity of these fluctuations. The

https://doi.org/10.1021/acsomega.4c10338
ACS Omega 2025, 10, 14980−14993

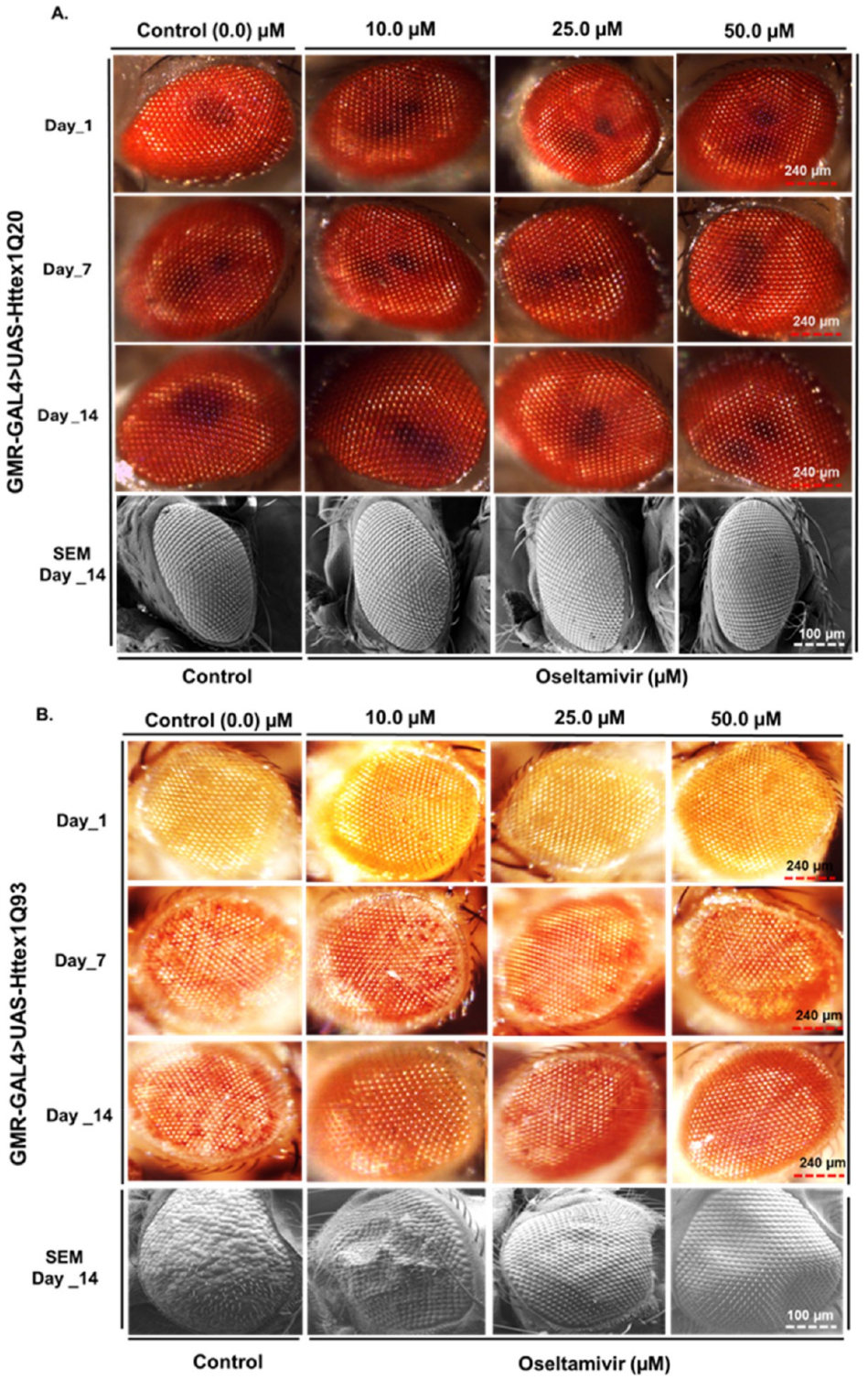

Figure 6. Figure depicts light microscopic and SEM images of eyes of adult flies (A) *UAS-Httex1Q20* and (B) *UAS-Httex1Q93*, both driven by the eye-specific driver line *GMR-GAL4*. The flies were fed with different concentrations (10.0, 25.0, and 50.0 μM) of Oseltamivir drug. (A) The control type did not show any significant change. Scale bar: 240 μm (light microscopic eye images), 100 μm (SEM images). (B) The pathogenic (Q93), however, showed improvement in terms of rough eye phenotype as well as pigmentation loss in accordance with the increasing drug concentration. Scale bar: 240 μm (light microscopic eye images), 100 μm (SEM images).

ligand's stable RMSD signifies the ligand's stable interaction with the RNA, forming a stable RNA-ligand complex, which is in conjunction with the overall results (Figure S7). The distance plot shows that throughout the simulation run, the distance between RNA and the docked ligand remains constant and is not subjected to periodic fluctuations (Figure S8).

The relative binding free energies calculated from the MD trajectory give further insights into the nature of the interactions between RNA and ligand. The MMPBSA calculation indicates

https://doi.org/10.1021/acsomega.4c10338
ACS Omega 2025, 10, 14980−14993

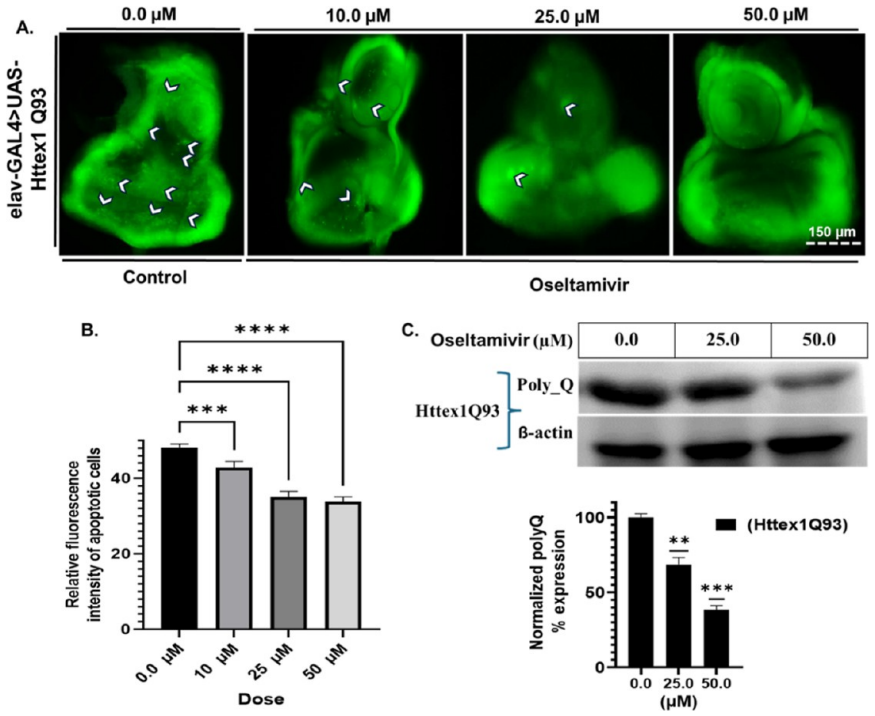

Figure 7. (A) Acridine orange (AO) staining of third-instar eye discs from *elav-GAL4 > UAS-Httex1Q93* larvae (pathogenic) displayed varying levels of cell death in accordance with the concentration. Arrows are indicative of cell death. (B) Relative fluorescence intensity of apoptotic cells also showed a significant decrease with the increasing concentration of Oseltamivir. Scale bar: 150 μm. Data represents mean ± SEM of values obtained in 5 larvae per condition (n = 5). Statistical significance: ****p < 0.0001; **p < 0.01, compared with control. Data analysis was performed using an analysis of variance (ANOVA), followed by Tukey's post hoc test. (C) Immunoblot analysis of Q93 protein isolated from *elav-GAL4 > UAS-Httex1Q93* fly lines treated with different drug concentrations. The bar graph depicts normalized PolyQ percentage expression with respect to different drug dosages.

the average binding affinity throughout the trajectory to be −12.95 kJ/mol (Table S3), which signifies strong interactions between the RNA and the ligand as observed through the docking studies where Oseltamivir binds to the Adenine base involved in the AA loop formation. The interaction is mainly dependent on electrostatic forces (Table S3).

Studying the Cellular Potency of Oseltamivir: Inhibition of RAN Translation. Previous studies have indicated that r(CAG)$_{exp}$, r(CCG)$_{exp}$, and r(CUG)$_{exp}$ lead to the formation of toxic homopolymeric protein aggregates through RAN translation.[15,16,29] Both in vitro and in vivo research suggest targeting polyQ-protein misfolding or polyQ-protein aggregation to be an effective approach for mitigating the severe effects of polyQ diseases.[30] Therefore, following the assessment of Oseltamivir's affinity and selectivity toward r(CAG)$_{exp}$ motifs within the target RNA, we aimed to evaluate its potential to alleviate cellular toxicity induced by r(C**A**G)$_{exp}$ RNA in HD cellular models. For this purpose, we employed an HD cell model utilizing a plasmid with EGFP gene fused to a huntingtin fragment corresponding to the exon 1 with 74 C**A**G repeats (EGFP-Q74). This plasmid was then used to transfect HEK-293 cells. Similar rational approaches are usually employed in designing selective compounds targeting various repeat-containing mRNAs implicated in similar repeat expansion neurodegenerative diseases.[29,31]

Both the enlarged polyQ (EGFP-HDQ74) and normal (EGFP-HDQ23) constructs were transiently transfected into HEK-293 cells. Transfected cells were subjected to varying concentrations of Oseltamivir before being utilized for micrograph analysis (Figure 5). A higher-magnification fluorescence examination was performed for Oseltamivir-treated cells expressing enlarged polyQ (EGFP-HDQ74) and normal (EGFP-HDQ23) proteins. Arrowheads show aggregate formation within the cells. As per the micrographs, as the concentration of Oseltamivir increases, the number of positive cells showing aggregation is reduced markedly. Additionally, a reduction in aggregate formation and cellular toxicity within a single cell is noted. Oseltamivir can reduce both the size and quantity of these aggregates within the cells (Figure 5A,B). Significant results were observed for the decrease in the aggregate formation within the positive cells at both 25 and 50 μM drug concentrations, respectively (Figure 5A,E).

Total cell lysates from similar sets of cells were then used for immunoblot analysis. The validity of the expression was confirmed using anti-PolyQ and anti-β actin antibodies. Our findings suggest that Oseltamivir reduces the proteotoxicity of enlarged polyQ proteins in cells (Figure 5C). Encouragingly, the treatment demonstrated a dose-dependent reduction in protein expression, with a 50% reduction observed at 25.0 μM and a further reduction to 75% at 50.0 μM (Figure 5D). Notably, no significant inhibition of control containing r(C**A**Gx23) repeats was observed at the same concentrations (Figure 5C). The blot images clearly show that polyQ expression significantly decreases with increasing Oseltamivir concentration, with p-values of 0.00010 for 50 μM and 0.0089 for 25 μM. The analysis of blot images was done using ImageJ software, followed by plotting a bar graph, and the significance of the decrease in polyQ expression was assessed (Figure 5D).

This suggests that Oseltamivir inhibits the translational machinery required for initiating noncanonical translation. Furthermore, the increased thermal stability of the r(C**A**G)$_{exp}$ hairpin induced by Oseltamivir binding corresponds to the

https://doi.org/10.1021/acsomega.4c10338
ACS Omega 2025, 10, 14980−14993

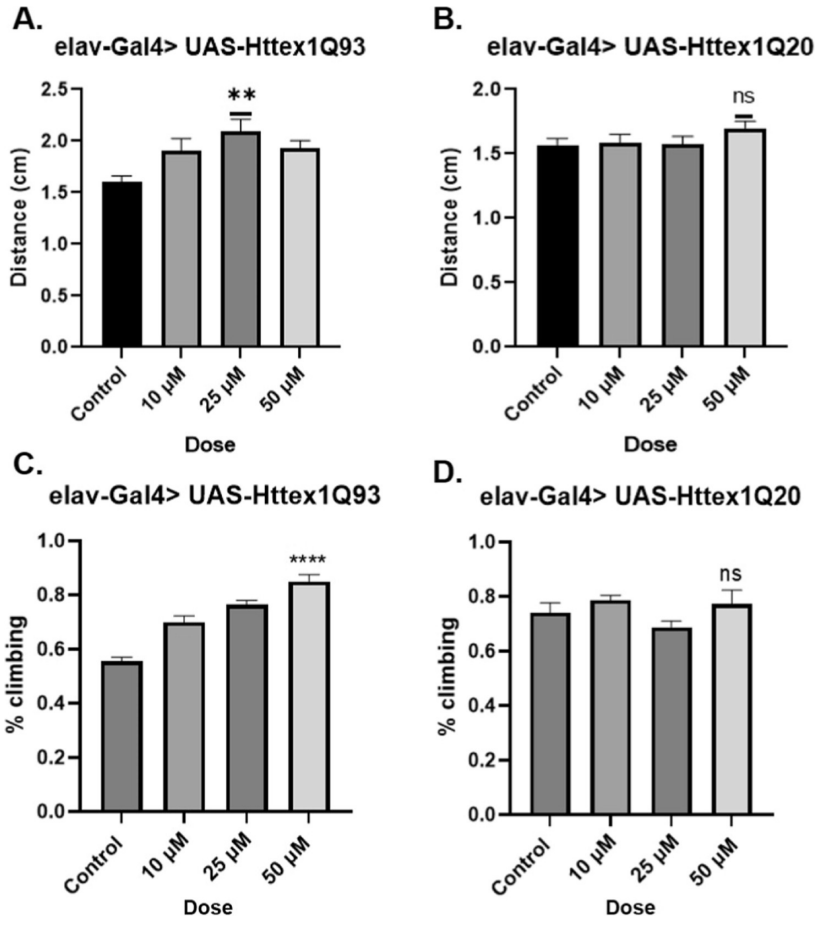

Figure 8. (A,B) Data represent the crawling ability of diseased and control third-instar larvae at varying drug concentrations. For each condition, the average of 10 larvae was calculated for two trials (n = 10). (C,D) Climbing assay for the adult flies. A comparison was made between same-age control and drug-treated flies. For each condition, the climbing ability of two groups of 10 flies was monitored for a total of 3 trials. Data analysis was performed using an analysis of variance (ANOVA) followed by Tukey's post hoc test; values represent mean ± SEM (****p < 0.0001; **p < 0.01; *p < 0.05 compared with control).

inhibitory effect on RAN translation. However, it is essential to note that various other factors contribute to RAN translation, and in this case, the increase in thermal stability of the CAG repeat RNA through Oseltamivir binding provides the necessary inhibitory effect on RAN translation. While our biophysical studies demonstrated nanomolar binding affinity, the effects observed in cellular systems were observed in the micromolar range, likely due to various off-target bindings affecting the cellular systems.

Oseltamivir Helps Alleviate the Rough Eye Phenotype and Pigment Loss Associated with polyQ-Induced Cytotoxicity in the *Drosophila* Model of HD. The expression of both *UAS-httex1Q20* and *UAS-httex1Q93* transgenes was activated in the compound eye of the flies using the pan-retinal *GMR-GAL4* driver line. The expression of mutant proteins through GMR leads to significant eye degeneration and noticeable external abnormalities (Figure 6). On treating the diseased flies with Oseltamivir, the external morphological abnormalities, including a rough eye phenotype, necrotic lesions, and pigment loss, showed an observable reduction with the increasing concentration of the Oseltamivir drug for the Q93 flies (Figure 6B). However, no significant change was observed for the control type (*UAS-Httex1Q20*) (Figure 6A). Roughness and pigmentation loss are indicative of gradual deterioration of the pigmented cells. Incorporation of the drug molecule in the food, however, clearly alleviates the impaired eye phenotype at days 7 and 14 posteclosion for the diseased phenotype (*UAS-httex1Q93*) in a dose-dependent manner.

The scanning electron microscopy (SEM) images of the control and drug-treated flies also showed a considerable improvement in eye morphology. The compound eye of *Drosophila* comprises approximately 800 ommatidia, which are organized in a stereotypical pattern. These hexagonal units exhibit precise arrangement with consistent spacing between the interommatidial bristles. The presence of disease-associated proteins or peptides in the eye results in alterations in these structured arrangements, exhibiting rough eye phenotype, a characteristic phenotype.[32] The treatment with Oseltamivir showed suppression of the rough eye phenotype, as visible through the SEM images. The overall eye appearance has improved upon dosing with higher concentrations of the drug molecules compared to the untreated ones. The structural abnormalities seen in the form of a rough eye for the untreated flies were found to be significantly reduced in the drug-treated flies, with the most substantial improvement observed in the flies fed with the highest dose (50 μM) of the drug (Figure 6B).

Oseltamivir Diminishes the Apoptotic Effects and Aggregation Inflicted by Poly-Q. Mutant huntingtin is known to induce neurodegeneration via a mechanism involving apoptosis. Expansion of CAG repeats leads to the initiation of

https://doi.org/10.1021/acsomega.4c10338
ACS Omega 2025, 10, 14980−14993

apoptosis.[33] Thus, Acridine Orange (AO) staining was performed to compare the intensity of cell death in both control and HD model flies, with or without the Oseltamivir treatment. AO staining provides a means to visualize the intensity of apoptosis via visualizing the acidic vesicular organelles in the tissues of transgenic flies.[34] The third-instar larval eye discs expressing *UAS-Httex1Q93* under the influence of neuronal-specific *elav-GAL4* were therefore treated as a control against the *Elav-GAL4 > UAS-Httex1Q93* treated with different concentrations of Oseltamivir. Eye discs of the untreated flies (Q93) clearly showed more apoptotic cells than drug-treated larval eye discs (Figure 7A,B). In fact, a significant reduction was clearly observed in the number of apoptotic cells when the drug concentration was increased. Analyzing the fluorescence intensity of eye discs stained with AO further validated that providing Oseltamivir-supplemented food significantly reduced the presence of AO-positive cells (Figure 7B). Thus, it can be decisively concluded that a potent Oseltamivir concentration significantly alleviates the cytotoxic and apoptotic effects triggered by PolyQ.

With significant improvements in the eye abnormalities, pigmentation, and apoptotic effects, we further investigated if our drug molecule leads to a reduction in the expression of toxic PolyQ proteins in the fly model of the disease. As per our findings, in addition to the cell-model-based results, immunoblot analysis from the HD-fly model also showed consistent results. Proteins were extracted from third-instar larvae reared under varying drug concentrations. Oseltamivir showed a significant reduction in the proteotoxicity of enlarged polyQ proteins in the *elav-GAL4* driven *UAS-httex1Q93* flies, with the increasing drug concentration. Even here, the treatment demonstrated a dose-dependent reduction in the protein expression, with around 32% reduction at 25.0 μM and around 62% reduction at 50.0 μM (Figure 7C). Whereas no significant reduction in the PolyQ protein expression was observed for the control fly line (*elav-GAL4 > UAS-httex1Q20*) (Figure S12). Figure S13 demonstrates a comparative description of 20 and 93 PolyQ protein's expression obtained from *UAS-httex1Q20* and *UAS-httex1Q93* fly lines, respectively.

Oseltamivir Improves the Locomotor Dysfunctions Caused by PolyQ. HD, specifically, is characterized by the degeneration of neurons in the striatum, a brain region responsible for regulating body movements.[35] Impaired neuronal functioning is therefore associated with deficiencies in mobility and climbing proficiency. To examine this, we assessed the impact of Oseltamivir on the motor abilities of flies expressing *Httex1Q20* and *Httex1Q93*, driven by the *elav-GAL4* (neuron-specific) driver line. Both *elav-GAL4 > Httex1Q20* and *elav-GAL4 > Httex1Q93* fly lines were cultured with varying concentrations of Oseltamivir. Larvae at the third instar stage then underwent a crawling assay to assess their locomotor functioning at the larval stage. Our findings suggest that feeding Oseltamivir enhanced the crawling ability of both Q93 and Q20 larvae (Figure 8A,B).

Similarly, to assess the motor functioning of the adult flies, we examined the climbing ability of same-age (7 day-old) male flies supplemented with different doses of Oseltamivir. The drug mainly did not significantly impact the locomotor functioning of control flies (*httex1Q20*) fed with drug-containing food since the larval stage. In contrast, a significant improvement in climbing ability was observed for the (*httex1Q93*) flies with the increasing concentration of the drug (Figure 8C,D). Thus, administering different concentrations of Oseltamivir relatively improved the locomotor ability of flies at both the larval and adult stages.

MATERIALS AND METHODS

Reagents. All cell culture reagents, chemical substances such as NaCl, KCl, $MgCl_2$, K_2HPO_4, KH_2PO_4, NaH_2PO_4, Na_2HPO_4, NaOH, HCl, Tris-base, EDTA, DMSO, APS, TEMED, acrylamide, bis-acrylamide, ethanol, isopropanol, 2-butanol, methanol, urea, Triton-X 100 and others, were sourced from Sigma-Aldrich Chemicals Ltd., based in St. Louis, Missouri, USA, and Sisco Research Laboratories Pvt. Ltd. in Mumbai, India. These were predominantly of HPLC purified or molecular grade quality. The dNTPs and rNTPs used for PCR and in vitro transcription reactions were also obtained from Sigma-Aldrich Chemicals Ltd. Additional materials such as Agarose, Luria broth, Luria agar, GC agar, and antibiotics like ampicillin, kanamycin, chloramphenicol, Taq polymerase, and others were procured from Himedia Laboratories in India. Standard plastic wares were supplied by Tarsons Products Pvt. Ltd. from Kolkata, India, while glasswares were sourced from Borosil.

Tissue culture plates and plasticware were obtained from Thermo Fisher and Tarsons. Anti-PolyQ and anti-β-actin antibodies were procured from Sigma-Aldrich and Santa Cruz Biotechnology, respectively. Lipofectamine 3000 was obtained from Invitro-Thermo Fisher. Calf thymus DNA (CT-DNA) was purchased from Sigma-Aldrich Chemicals Ltd.

RNA Oligo Synthesis Using T7-RNA Polymerase-Mediated In Vitro Transcription Reactions. As previously described,[1] different RNA sequences employed in biophysical investigations were prepared using runoff transcription and artificial DNA templates. In brief, T7 RNA polymerase was used to transcribe synthetic DNA templates, and 15% Urea-PAGE was used to denature the transcribed products to purify them. RNA was extracted using 0.3 M NaCl by tumbling down for an entire night at 4 °C after UV shadowing.

Fluorescence Titration Assay. The fluorescence binding assays were conducted at room temperature using Corning half area 96-well black plates.[27] Readings were taken using a Synergy H1 multimode microplate reader postassay. 50 μM of RNAs were serially diluted with the last well as a blank. Each sample was run in triplicate. The excitation and emission wavelengths for these molecules were predetermined. To ensure consistency, each well in the assay contained an equal concentration of the drug molecule. Data analysis was conducted using SigmaPlot 12.0 software (Systat Software, Chicago, USA) employing a binding equation for data fitting: one-mode data fits were used.

$$f = \frac{B_{max} \times \mathrm{abs}(x)}{K_{d_1} \times \mathrm{abs}(x)} + \frac{B_{max_2} \times \mathrm{abs}(x)}{K_{d_2} \times \mathrm{abs}(x)}$$

Here, B_{max} represents the maximum number of binding sites, and K_d denotes the equilibrium dissociation constant.

Circular Dichroism Spectroscopy. This experiment utilized a JASCO J-815 Spectropolarimeter, and a constant temperature of 298 K was maintained using a Peltier junction temperature controller. A steady flow of dry nitrogen gas was directed into the chamber holding the cuvette to prevent water condensation on the exterior of the cuvette, with spectra recorded in a cuvette of 1 mm path length at regular intervals of 0.1 nm and averaged over three scans. RNA samples were maintained at constant concentrations of 10 μM, while the concentration of Oseltamivir drug varied in 10 mM potassium phosphate buffer, at pH 7.2, and 50 mM KCl. To ensure

https://doi.org/10.1021/acsomega.4c10338
ACS Omega 2025, 10, 14980−14993

accuracy, a blank spectrum of the buffer (1× KPO_4, KCl, and MQ water) was recorded before each measurement and subtracted from the sample's CD spectrum, as explained previously.[29] Data analysis was performed using SigmaPlot 13.0, allowing for a detailed interpretation of RNA-ligand interactions and their stabilizing or destabilizing effects on loop structures.

Thermal Denaturation Experiments. Thermal denaturation experiments were conducted utilizing a J-815 Spectropolarimeter (JASCO) coupled with a Peltier junction temperature controller. The RNA samples were subjected to gradual heating from 25 to 95 °C, while monitoring the absorbance at 260 nm at a rate of 1 °C/min, both in the absence and presence of Oseltamivir, up until a D/N ratio of 3.0. The changes in normalized absorbance at 260 nm versus temperature were analyzed and plotted using SigmaPlot 12.0 software.

Electrophoretic Mobility Shift Assay. The RNA samples under study were dissolved in a 1× KPO_4 buffer containing 50 mM KCl. These samples were incubated with varying concentrations of Oseltamivir, ranging from 0.0 to 3.0 mM, and allowed to equilibrate for 30 min at room temperature, followed by resolution on a 3% agarose gel and visualization through staining with ethidium bromide. The results of the EMSA were documented and analyzed using ImageQuant LAS4000 (GE Healthcare).

PCR Stop Assay. Templates for AA × 1 (5′-GGA GAG GGU UUA AUC AGU ACG AAA GUA CAG AUU GGA UCC GCA AGG-3′), AA × 6 (5′-GGA GAG GGU UUA AUC AGC AGC AGC AGC AGC AGU ACG AAA GUA CAG CAG CAG CAG CAG CAG AUU GGA UCC GCA AGG-3′) and complementary sequence (5′-GGC CGG ATC CTA ATA CGA CTC ACT ATA GGG AGA GGG TTT AAT-3′) were procured from Sigma-Aldrich Chemicals Ltd., based in USA. The master mix for the PCR stop assay contained 1× PCR reaction buffer, 8 mM $MgCl_2$, 1 μM oligonucleotides, 1 mM dNTPs, 2.5 units of Taq polymerase, and serial dilutions of Oseltamivir ranging from 0 to 3 mM. The PCR cycle was as follows: 95 °C for 3 min, followed by 30 cycles of 95 °C for 30 s, 70 °C for 30 s, 72 °C for 1 min, a final extension at 72 °C for 10 min, and finally holding at 4 °C for infinity. The products were mixed with 6× loading dye, resolved on a 3% acrylamide-resolving gel without any added cations, and stained with ethidium bromide. The gel images were captured using ImageQuant LAS 4000 and analyzed using ImageJ.

Isothermal Titration Calorimetry. All ITC studies were conducted using the MicroCal iTC200 system from GE Healthcare, Biosciences Ltd., Sweden, following previously established protocols. RNAs were prepared in a 1× KPO_4 buffer containing 50 mM KCl at a pH of 7.2. The RNA was placed in the ITC cell, and compounds were titrated using a syringe containing Oseltamivir, initiating with an injection of 0.4 μL with 60 s initial delays. Throughout the experiment, the sample was stirred at 1000 rpm, and the reference power was maintained at 8 μcal/s. A total of 22 injections, each measuring 1.66 μL of Oseltamivir, were administered to the cells containing the RNA. Data fitting was performed using a two-site binding model to determine the dissociation constant, utilizing Origin Scientific software version 7 (Microcal Software Inc., Northampton, MA, US) provided with the instrument.

Nuclear Magnetic Resonance Spectroscopy. NMR experiments were conducted for r(C**A**G)$_6$ repeat RNA. Bruker NMR 400 Hz instrument, equipped with a 5 mm broad-band inverse probe capable of delivering z-field gradients was used. Drug/RNA samples were prepared in a 1× KPO_4 buffer with 10% D_2O, DSS (4,4-dimethyl-4-silapentane-1-sulfonic acid) used as the NMR sample reference. NMR broadening experiments were performed by gradually adding RNA dissolved in H_2O/D_2O solvent in a 9:1 ratio utilized to lock the radio frequency throughout the titration studies. 64K data points were recorded for 1D proton NMR spectra, with a relaxation delay of 8 s, 64−170 scans at 298 K, and a digital resolution of 0.15−0.3 Hz/point applied. The resulting NMR spectra were processed for baseline and phase correction. Tuning, matching, and shimming were carried out to ensure consistency in sample handling across successive titrations. Topspin version 3.5 was employed to process, integrate, and analyze the NMR data.

In Silico Molecular Docking. The three-dimensional structure of C**A**G duplex RNA (Protein Data Bank ID: 4J50) served as the initial model for receptor preparation. Structure preparation for docking analysis was carried out using Auto Dock tools. Following receptor preparation, the ligand 3D structure was downloaded from the PubChem database in sdf format (PubChem CID ID: 65028). Further ligand preparation was meticulously executed using Discovery Studio 3.5 (San Diego, Dassault Systèmes, USA), a sophisticated molecular modeling and simulation platform.[28] After receptor and ligand preparation, docking studies were conducted using Auto Dock Vina (The Scripps Research Institute, La Jolla, CA, USA). The outcomes of the docking studies were primarily analyzed based on the binding affinities of the ligand to the duplex RNA.

Molecular Dynamic Simulation Studies. The stability of the generated RNA structure and the docked complexes was further evaluated by an all-atom MD simulation using GROMACS 2023.3. The topology details for RNA were acquired using the CHARMM27 all-atom force field. The complexes were solvated by a TIP3P water model in a cubic box. They were then neutralized by adding a suitable amount of counterions, with the concentration of KCl set to 0.15 M. To avoid atomic clashes in the system, the system's energy was minimized using the steepest descent method, and the maximum forces were converged below 1000 kJ/mol/nm. Electrostatics were treated with Particle Mesh Ewald, and the cutoff for both Coulomb and van der Waals interactions was 1.0 nm. Further *NVT*, and *NPT* ensembles run for 1 ns each were carried out at a temperature of 298.15 K and a pressure of 1 bar, respectively. For these cases, the modified Berendsen thermostat was used to regulate temperature, and a Parinello-Rahman barostat was used to regulate pressure equilibrations. Finally, 100 ns production run was executed. A time step of 2 fs was used, and the frames were updated every 5000 steps. The RMSD of the RNA alone and RNA-ligand complex were calculated after square fitting to the system.

Binding Free Energy Calculation. The binding free energy calculations in the dynamic state were calculated using the molecular mechanics Poisson−Boltzmann surface area (MMPBSA) method and the gmx_MMPBSA tool. A total of 9999 frames of the 100 ns simulation were subjected to the calculations. The calculations were carried out at a temperature of 298.15 K, and the PB radii was 4 nm. In this method, all individual energy components are calculated, including polar and nonpolar solvation energy, the van der Waals forces, and the electrostatic contacts of the complex, as well as the receptor and ligand individually. The final free-binding energy for a complex can then be estimated by the following:

$$\Delta G_{bind} = \langle G_{COM} \rangle - \langle G_{REC} \rangle - \langle G_{LIG} \rangle$$

https://doi.org/10.1021/acsomega.4c10338
ACS Omega 2025, 10, 14980−14993

ΔG_{bind} can also be represented as $\Delta G_{bind} = \Delta H - T\Delta S$. Where ΔH corresponds to the enthalpy of binding and $-T\Delta S$ to the conformational entropy after ligand binding. When the entropic term is dismissed, the computed value is the effective free energy, which is usually sufficient for comparing the relative binding free energies of related ligands.

Cell Culture and Protein Aggregate Visualization. The HEK-293 cell line was cultured at 37 °C in a 5% CO_2 environment using DMEM medium supplemented with 10% heat-inactivated FBS and 100 μg/mL antibiotics. Cells were cultured on chamber slides as well as 6-well tissue culture plates. At a 60% confluence stage, transient transfections were performed using plasmids (EGFP-HDQ74 and EGFP-HDQ23). Cells were then treated without the drug as a control and with different concentrations of Oseltamivir for 24 h each. After washing cells with PBS, they were fixed with 4% paraformaldehyde for 15 min. Fluorescence microscopy was utilized to observe polyQ protein aggregates. Confocal microscopy was utilized to visualize protein aggregation at a higher magnification. Several similar sets of cells were utilized for aggregation count analysis, with approximately 500 transfected cells in each set.

Western Blot Analysis. HEK-293 cells cultured in a 6-well plate were transfected with EGFP-HDQ74 and EGFP-HDQ23 plasmids and exposed to Oseltamivir for 24 h, as described previously.[27] Cell lysates were gathered using RIPA lysis buffer and separated using SDS page at 80 V, then transferred onto a nitrocellulose membrane in transfer buffer containing methanol for 80 min at 4 °C. Blots were blocked for 1 h in 5% skimmed milk in TBST (50 mM Tris, pH 7.4, 0.15 M NaCl, 0.05% Tween), then probed overnight at 4 °C with primary antibodies at a 1:1000 dilution in TBST. Horseradish peroxidase-conjugated secondary antibodies were subsequently used at a 1:10000 dilution prepared in TBST. The Luminata Crescendo Western HRP substrate was utilized for blot detection. The gel images were captured using the Gel Documentation System (Bioprint) and analyzed using ImageJ.

***Drosophila* Stocks and Dietary Conditions.** The transgenic fly lines expressing the 20 polyQ repeats (UAS-Q20) and the mutant fly lines expressing the 93 polyQ repeats encoded by exon 1 of the HTTgene (*UAS-httex1Q93* or *UAS-Q93*)[36] were kind gift from Prof. Pradip Sinha (IIT Kanpur). The pan-neuronal driver line *elav-GAL4*[37] and the eye-specific driver line that expresses in the eye-imaginal discs of the larvae and in the adult eye (*GMR-GAL4*)[38] were kindly provided by Dr. Anand K. Tiwari (IAR Gandhinagar). Males of all the transgenic lines used in the study were crossed with virgins of *elav-GAL4* and *GMR-GAL4* to drive their expression in the fly brain and the eye-imaginal discs, respectively.[39] The flies were maintained on a typical cornmeal-agar diet at a temperature of 25 ± 1 °C with consistent light−dark cycles and humidity ranging from 70% to 80%. Oseltamivir was added to the fly food at concentrations of 10, 25, and 50 μM to rear experimental larvae or flies. Control groups were raised on regular food without the drug at a constant temperature of 25 °C.

Rough Eye Phenotype Assessment. The rough eye phenotype of flies expressing *Httex1Q93* under the control of *GMR-GAL4* was evaluated. These flies were cultured at 25 °C on standard food and food supplemented with either 10, 25, and 50 μM drug compounds. The outer surface of the fly eye was scrutinized using a Leica S8Apo microscope on days 1, 7, and 14 after emergence. A total of 20 flies were examined for each condition.[26]

Scanning Electron Microscopy. Critical point dried (CPD) method was used to prepare samples for attaining high-magnification analysis through SEM.[40] First, whole flies were immersed in a fixative composed of (1% glutaraldehyde, 1% formaldehyde, and 1 M sodium cacodylate (pH 7.2)) for 2 h. Further, to submerse the flies in the fixative, single drops of 0.2% Tween 20 (diluted in H_2O) were used. This was followed by rinsing in H_2O. Then, the flies were dehydrated in an ethanol series (once in 25%, 50%, and 75% ethanol and twice in 100% ethanol), each for 12 h, at room temperature. The flies were then fixed and images were taken followed by CPD and sputter-coat.[41]

Negative Geotaxis (*Drosophila* Climbing) Assay. To evaluate the locomotor capabilities of flies, a negative geotaxis assay was conducted. Each condition was tested with two groups of 10 flies each, across a total of three trials conducted in the designated tube. Flies were introduced into a vertical column measuring 25 cm in length and 1.5 cm in diameter. After gently tapping the column thrice, flies that crossed the 10 cm mark and those remaining at the bottom were counted separately.[26] The outcome was quantified as the number of flies surpassing a specified distance within a 15 s interval.

Crawling Assay. To measure the crawling ability, a Petri dish measuring 100 mm × 10 mm and made of 3.3% agar served as the apparatus. Within this dish, a track measuring 2 mm wide, 30 mm long, and 5 mm deep was formed, as described previously.[26] The locomotion of each third-instar larva placed in the track was observed for 20 s, with 5 larvae per condition monitored across three trials.

Dead Cell Detection. Acridine Orange (AO), a vital dye is used for the identification of the apoptotic cells. Living cells being selectively permeable, exclude the dye. Dead cells, however, lose their permeability barrier, and the dye molecules easily permeate and intercalate between the base pairs of dsDNA, causing it to fluoresce green. Here, the Acridine Orange (AO) staining was used to observe the presence of apoptotic cells in the eye imaginal discs of the third-instar larvae. Third instar larval eye imaginal discs were first dissected in 1× PBS. The tissues were then incubated in 5 μg/mL acridine orange (Sigma Cat. no. A6014) solution for 2 min, followed by washing in 1× PBS, and were then mounted in 1× PBS. The tissues were then immediately photographed using a fluorescent microscope with a minimum of 5 discs captured for each condition.

Western Blot Analysis. Western Blot was carried out as described earlier. Here, the proteins were isolated from flies treated with different drug concentrations. Equal protein amounts were loaded and separated via 10% SDS-polyacrylamide gel electrophoresis, followed by transfer to a PVDF membrane. The membrane was blocked with a 5% skimmed milk (in TBST) solution and then incubated with primary antibody at a 1:1000 dilution overnight. Secondary antibodies conjugated with horseradish peroxidase were used at a 1:10,000 dilution in TBST. For blot detection, the Luminata Crescendo Western HRP substrate was applied. Gel images were captured with the Bioprint Gel Documentation System and analyzed using ImageJ software.

CONCLUSIONS

Efficient and adaptable therapeutics for CAG repeats are crucial for addressing conditions like HD and SCA. Targeting expanded CAG repeat RNA with naturally occurring small molecules holds promise for developing potential therapeutic leads. In managing neurological disorders, optimizing long-term therapy

https://doi.org/10.1021/acsomega.4c10338
ACS Omega 2025, 10, 14980−14993

with lower doses is crucial, highlighting the advantages of U.S. FDA-approved small molecules. Our study demonstrates the specific binding of Oseltamivir toward the CAG repeat RNA, assessed through various biophysical techniques such as ITC, CD, EMSA, and NMR spectroscopy, with the binding mode characterized via molecular docking. Furthermore, the effectiveness of Oseltamivir in mitigating disease pathology in the cellular HD model suggests promising therapeutic potential. Further analysis of the effectiveness of Oseltamivir using the *Drosophila* HD model also showed favorable findings. However, further research involving murine animal models is needed to elucidate Oseltamivir's mechanism of action in a more precise manner. Overall, the study provides compelling evidence for the therapeutic potential of Oseltamivir in targeting expanded CAG repeat RNAs implicated in neurological disorders.

■ ASSOCIATED CONTENT

Supporting Information

The Supporting Information is available free of charge at https://pubs.acs.org/doi/10.1021/acsomega.4c10338.

This section has all the experimental binding data (fluorescence titration curve, ITC), MD simulation plots, EMSA, PCR stop assay plots, images of eye discs showing the effect of Oseltamivir on cell death, mass spectrometry of Oseltamivir, drug-treated immune blot images of poly-Q20 and blots with comparative depiction of Q93 and Q20 polyQ protein (PDF)

■ AUTHOR INFORMATION

Corresponding Author

Amit Kumar − *Department of Biosciences and Biomedical Engineering, Indian Institute of Technology Indore, Indore 453552, India;* orcid.org/0000-0002-5913-4308; Email: amitk@iiti.ac.in

Authors

Krishna Singh − *Department of Biosciences and Biomedical Engineering, Indian Institute of Technology Indore, Indore 453552, India*

Kanav Gupta − *Department of Biosciences and Biomedical Engineering, Indian Institute of Technology Indore, Indore 453552, India*

Sakshi Shukla − *Department of Biosciences and Biomedical Engineering, Indian Institute of Technology Indore, Indore 453552, India*

Aditi Pramod Kumari − *Department of Biosciences and Biomedical Engineering, Indian Institute of Technology Indore, Indore 453552, India*

Complete contact information is available at: https://pubs.acs.org/10.1021/acsomega.4c10338

Author Contributions

†K.S., K.G., and S.S. contributed equally to this work. A.K. conceived and designed the experiments. K.S., K.G., S.S. and K.A.P performed the biophysical experiments. K.S., S.S., and K.A.P. performed cell and Drosophila-based experiments. K.S., S.S., and A.K. analyzed the data and wrote the manuscripts.

Funding

A.K. would like to acknowledge SERB, Department of Science & Technology, New Delhi, for the CRG/2023/002978 grant and the DST-FIST Project (SR/FST/LS-I/2020/621).

Notes

The authors declare no competing financial interest.

■ ACKNOWLEDGMENTS

K.S. would like to acknowledge the CSIR-UGC, Govt. of India, New Delhi, K.G. to the Department of Biotechnology, Govt. of India, S.S. and A.P.K. to the Ministry of Human Resource Development, Govt. of India, for their individual fellowships. Figures employed the BioRender program. Authors acknowledge the Sophisticated Instrumentation Facility at IIT Indore for NMR, Confocal microscopy, and CD experiments. We sincerely thank A. Tunnacliffe (Department of Chemical Engineering and Biotechnology, University of Cambridge, Cambridge, UK) for EGFP-HDQ23 and EGFP-HDQ74 constructs.

■ ABBREVIATIONS

HD	Huntington's disease
SCA	Spinocerebellar Ataxia
TREDs	trinucleotide repeat expansion disorders
PolyQ	poly-glutamine

■ REFERENCES

(1) Cooper, T. A.; Wan, L.; Dreyfuss, G. RNA and disease. *Cell* **2009**, *136*, 777−793.

(2) Paulson, H. Repeat expansion diseases. *Handb. Clin. Neurol.* **2018**, *147*, 105−123.

(3) Kozlowski, P.; de Mezer, M.; Krzyzosiak, W. J. Trinucleotide repeats in human genome and exome. *Nucleic Acids Res.* **2010**, *38*, 4027−4039.

(4) McMurray, C. T. Mechanisms of trinucleotide repeat instability during human development. *Nat. Rev. Genet.* **2010**, *11*, 786−799.

(5) Orr, H. T.; Zoghbi, H. Y. Trinucleotide repeat disorders. *Annu. Rev. Neurosci.* **2007**, *30*, 575−621.

(6) MacDonald, M. E.; Ambrose, C. M.; Duyao, M. P.; Myers, R. H.; Lin, C.; Srinidhi, L.; Barnes, G.; Taylor, S. A.; James, M.; Groot, N.; MacFarlane, H.; Jenkins, B.; Anderson, M. A.; Wexler, N. S.; Gusella, J. F.; Bates, G. P.; Baxendale, S.; Hummerich, H.; Kirby, S.; North, M.; Youngman, S.; Mott, R.; Zehetner, G.; Sedlacek, Z.; Poustka, A.; Frischauf, A.-M.; Lehrach, H.; Buckler, A. J.; Church, D.; Doucette-Stamm, L.; O'Donovan, M. C.; Riba-Ramirez, L.; Shah, M.; Stanton, V. P.; Strobel, S. A.; Draths, K. M.; Wales, J. L.; Dervan, P.; Housman, D. E.; Altherr, M.; Shiang, R.; Thompson, L.; Fielder, T.; Wasmuth, J. J.; Tagle, D.; Valdes, J.; Elmer, L.; Allard, M.; Castilla, L.; Swaroop, M.; Blanchard, K.; Collins, F. S.; Snell, R.; Holloway, T.; Gillespie, K.; Datson, N.; Shaw, D.; Harper, P. S. A novel gene containing a trinucleotide repeat that is expanded and unstable on Huntington's disease chromosomes. *Cell* **1993**, *72*, 971−983.

(7) Zoghbi, H. Y.; Orr, H. T. Glutamine repeats and neurodegeneration. *Annu. Rev. Neurosci.* **2000**, *23*, 217−247.

(8) Jiang, A.; Handley, R. R.; Lehnert, K.; Snell, R. G. From pathogenesis to therapeutics: a review of 150 years of Huntington's disease research. *Int. J. Mol. Sci.* **2023**, *24*, 13021.

(9) Passoni, A.; Favagrossa, M.; Colombo, L.; Bagnati, R.; Gobbi, M.; Diomede, L.; Birolini, G.; Di Paolo, E.; Valenza, M.; Cattaneo, E.; Salmona, M. Efficacy of cholesterol nose-to-brain delivery for brain targeting in Huntington's disease. *ACS Chem. Neurosci.* **2020**, *11*, 367−372.

(10) Myers, R. H. Huntington's disease genetics. *NeuroRX* **2004**, *1*, 255−262.

(11) Bates, G. P.; Dorsey, R.; Gusella, J. F.; Hayden, M. R.; Kay, C.; Leavitt, B. R.; Nance, M.; Ross, C. A.; Scahill, R. I.; Wetzel, R.; Wild, E. J.; Tabrizi, S. J. Huntington disease. *Nat. Rev. Dis. Primers* **2015**, *1*, 15005.

(12) Roos, R. A. C. Huntington's disease: a clinical review. *Orphanet J. Rare Dis.* **2010**, *5*, 40.

(13) Malik, I.; Kelley, C. P.; Wang, E. T.; Todd, P. K. Molecular mechanisms underlying nucleotide repeat expansion disorders. *Nat. Rev. Mol. Cell Biol.* **2021**, *22*, 589−607.
(14) Tenchov, R.; Sasso, J. M.; Zhou, Q. A. Polyglutamine (PolyQ) diseases: navigating the landscape of neurodegeneration. *ACS Chem. Neurosci.* **2024**, *15*, 2665.
(15) Bañez-Coronel, M.; Ayhan, F.; Tarabochia, A. D.; Zu, T.; Perez, B. A.; Tusi, S. K.; Pletnikova, O.; Borchelt, D. R.; Ross, C. A.; Margolis, R. L.; Yachnis, A. T.; Troncoso, J. C.; Ranum, L. P. W. RAN translation in Huntington disease. *Neuron* **2015**, *88*, 667−677.
(16) Grima, J. C.; Daigle, J. G.; Arbez, N.; Cunningham, K. C.; Zhang, K.; Ochaba, J.; Geater, C.; Morozko, E.; Stocksdale, J.; Glatzer, J. C.; Pham, J. T.; Ahmed, I.; Peng, Q.; Wadhwa, H.; Pletnikova, O.; Troncoso, J. C.; Duan, W.; Snyder, S. H.; Ranum, L. P. W.; Thompson, L. M.; Lloyd, T. E.; Ross, C. A.; Rothstein, J. D. Mutant Huntingtin disrupts the nuclear pore complex. *Neuron* **2017**, *94*, 93−107.
(17) Zanforlin, E.; Zagotto, G.; Ribaudo, G. The medicinal chemistry of natural and semisynthetic compounds against Parkinson's and Huntington's diseases. *ACS Chem. Neurosci.* **2017**, *8*, 2356−2368.
(18) Lum, P. T.; Sekar, M.; Gan, S. H.; Bonam, S. R.; Shaikh, M. F. Protective effect of natural products against Huntington's disease: an overview of scientific evidence and understanding their mechanism of action. *ACS Chem. Neurosci.* **2021**, *12*, 391−418.
(19) Aharony, I.; Ehrnhoefer, D. E.; Shruster, A.; Qiu, X.; Franciosi, S.; Hayden, M. R.; Offen, D. A Huntingtin-based peptide inhibitor of caspase-6 provides protection from mutant Huntingtin-induced motor and behavioral deficits. *Hum. Mol. Genet.* **2015**, *24*, 2604−2614.
(20) Marelli, C.; Maschat, F. The P42 peptide and peptide-based therapies for Huntington's disease. *Orphanet J. Rare Dis.* **2016**, *11*, 24.
(21) Disney, M. D. Rational design of chemical genetic probes of RNA function and lead therapeutics targeting repeating transcripts. *Drug Discovery Today* **2013**, *18*, 1228−1236.
(22) Nakatani, K.; Hagihara, S.; Goto, Y.; Kobori, A.; Hagihara, M.; Hayashi, G.; Kyo, M.; Nomura, M.; Mishima, M.; Kojima, C. Small-molecule ligand induces nucleotide flipping in (Cag)n trinucleotide repeats. *Nat. Chem. Biol.* **2005**, *1*, 39−43.
(23) Zhao, Y.; Rao, P. P. N. Small molecules N-phenylbenzofuran-2-carboxamide and N-phenylbenzo[b]thiophene-2-carboxamide promote beta-amyloid (Aβ42) aggregation and mitigate neurotoxicity. *ACS Chem. Neurosci.* **2023**, *14*, 4185−4198.
(24) Chuang, P.-H.; Tzang, B.-S.; Tzang, C.-C.; Chiu, C.-C.; Lin, C.-Y.; Hsu, T.-C. Impact of oseltamivir on the risk of cancer. *Front. Oncol.* **2024**, *14*, 1329986.
(25) Huang, P.-J.; Chiu, C.-C.; Hsiao, M.-H.; Yow, J. Le.; Tzang, B.-S.; Hsu, T.-C. Potential of antiviral drug oseltamivir for the treatment of liver cancer. *Int. J. Oncol.* **2021**, *59*, 109.
(26) Chongtham, A.; Agrawal, N. Curcumin modulates cell death and is protective in Huntington's disease model. *Sci. Rep.* **2016**, *6*, 18736.
(27) Khan, E.; Tawani, A.; Mishra, S. K.; Verma, A. K.; Upadhyay, A.; Kumar, M.; Sandhir, R.; Mishra, A.; Kumar, A. Myricetin reduces toxic level of CAG repeats RNA in Huntington's disease (HD) and spino cerebellar ataxia (SCAs). *ACS Chem. Biol.* **2018**, *13*, 180−188.
(28) Ding, Y.; Zhang, Z.-F.; Dai, X.-Q.; Li, Y. Myricetin protects against cytokine-induced cell death in RIN-m5f β cells. *J. Med. Food* **2012**, *15*, 733−740.
(29) Verma, A. K.; Khan, E.; Mishra, S. K.; Jain, N.; Kumar, A. Piperine modulates protein mediated toxicity in fragile X-associated tremor/ataxia syndrome through interacting expanded CGG repeat (r(CGG)-(exp)) RNA. *ACS Chem. Neurosci.* **2019**, *10*, 3778−3788.
(30) Tanimoto, S.; Okumura, H. Why is arginine the only amino acid that inhibits polyglutamine monomers from taking on toxic conformations? *ACS Chem. Neurosci.* **2024**, *15*, 2925.
(31) Sellier, C.; Freyermuth, F.; Tabet, R.; Tran, T.; He, F.; Ruffenach, F.; Alunni, V.; Moine, H.; Thibault, C.; Page, A.; Tassone, F.; Willemsen, R.; Disney, M. D.; Hagerman, P. J.; Todd, P. K.; Charlet-Berguerand, N. Sequestration of DROSHA and DGCR8 by expanded CGG RNA repeats alters microRNA processing in fragile X-associated tremor/ataxia syndrome. *Cell Rep.* **2013**, *3*, 869−880.
(32) Prüßing, K.; Voigt, A.; Schulz, J. B. Drosophila melanogaster as a model organism for Alzheimer's disease. *Mol. Neurodegener.* **2013**, *8*, 35.
(33) Fan, H.-C.; Ho, L.-I.; Chi, C.-S.; Chen, S.-J.; Peng, G.-S.; Chan, T.-M.; Lin, S.-Z.; Harn, H.-J. Polyglutamine (PolyQ) diseases: genetics to treatments. *Cell Transplant.* **2014**, *23*, 441−458.
(34) Thomé, M. P.; Filippi-Chiela, E. C.; Villodre, E. S.; Migliavaca, C. B.; Onzi, G. R.; Felipe, K. B.; Lenz, G. Ratiometric analysis of Acridine Orange staining in the study of acidic organelles and autophagy. *J. Cell Sci.* **2016**, *129*, 4622−4632.
(35) Abraira, V. E.; et al. The cellular and synaptic architecture of the mechanosensory dorsal horn. *Cell* **2017**, *168* (1−2), 295−310.e19.
(36) Kazemi-Esfarjani, P.; Benzer, S. Genetic suppression of polyglutamine toxicity in Drosophila. *Science* **2000**, *287*, 1837−1840.
(37) Koushika, S. P.; Lisbin, M. J.; White, K. ELAV, a Drosophila neuron-specific protein, mediates the generation of an alternatively spliced neural protein isoform. *Curr. Biol.* **1996**, *6*, 1634−1641.
(38) Ray, M.; Lakhotia, S. C. The commonly used eye-specific sev-GAL4 and GMR-GAL4 drivers in Drosophila melanogaster are expressed in tissues other than eyes also. *J. Genet.* **2015**, *94*, 407−416.
(39) Onkar, A.; Sheshadri, D.; Rai, A.; Gupta, A. K.; Gupta, N.; Ganesh, S. Increase in brain glycogen levels ameliorates Huntington's disease phenotype and rescues neurodegeneration in Drosophila. *Dis. Models Mech.* **2023**, *16*, dmm050238.
(40) Kimmel, C. B.; Ballard, W. W.; Kimmel, S. R.; Ullmann, B.; Schilling, T. F. Stages of embryonic development of the zebrafish. *Dev. Dyn.* **1995**, *203*, 253−310.
(41) Wolff, T. Preparation of Drosophila eye specimens for scanning electron microscopy. *Cold Spring Harb. Protoc.* **2011**, *2011*, 1383−1385.

https://doi.org/10.1021/acsomega.4c10338
ACS Omega 2025, 10, 14980−14993